Multifaceted Simulations Reproducing Experimental Results from the 1.5 MW 140 GHz Pre-Prototype Gyrotron for W7-X

Konstantinos A. Avramidis, Zisis C. Ioannidis, Stefan Illy, Jianbo Jin, Tobias Ruess, Gaetano Aiello, Manfred Thumm, *Life Fellow*, *IEEE*, and John Jelonnek, *Senior Member*, *IEEE*

1

***Abstract*—A multifaceted simulation procedure, addressing the electron beam properties, the beam-wave interaction, and the internal losses, has been used for the simulation of the experimental operation of a 1.5 MW 140 GHz short-pulse pre-prototype gyrotron. The pre-prototype is related to the development of 1.5 MW gyrotrons for the upgrade of the Electron Cyclotron Resonance Heating system at the stellarator W7-X. A very good reproduction of experimental results has been achieved by simulation, without resorting to arbitrary speculations. This validated the numerical tools as well as the design and fabrication of the short-pulse pre-prototype, which fully reached the target of efficient 1.5 MW operation in ms pulses. Special attention has been given in simulating the possibility of parasitic after-cavity interaction in the gyrotron launcher. Also, parasitic backward-wave excitation in the gyrotron cavity has been demonstrated by simulation, at a frequency and voltage range in agreement with experimentally observed parasitic oscillations. This offers an additional possibility with respect to the origin of deleterious parasitic oscillations in high-power gyrotrons, which are usually attributed mainly to the gyrotron beam tunnel.**

***Index Terms*—Gyrotron, Controlled fusion, Stellarator Wendelstein 7-X, ECRH, Gyrotron simulation**

I. Introduction

THE stellarator Wendelstein 7-X (W7-X) started operation in late 2015 and has up to now achieved outstanding results [1-4], including the highest fusion triple product achieved for stellarators, pulse lengths up to 100 s, and efficient compensation of the bootstrap current in the plasma by Electron Cyclotron Current Drive. The operation was sustained by a highly reliable Electron Cyclotron Resonance Heating (ECRH) system of 10 MW installed power, produced by ten 1 MW 140 GHz gyrotrons [5]. The experiments made also clear that, for advanced operating regimes at high plasma beta and low collisionality (as expected in reactor-scale devices), the ECRH system needs to be upgraded to higher power, in order to increase the heating power into the plasma. The roadmap for this upgrade incorporates the development of a prototype Continuous-Wave (CW) 1.5 MW, 140 GHz gyrotron, which will be followed by three series tubes. The development of the CW prototype by the industrial partner (Thales, Vélizy-Villacoublay, France) is ongoing, with a planned delivery of the tube in October 2021 [6].

The electron optics and RF design of the 1.5 MW gyrotron was realized by the Karlsruhe Institute of Technology (KIT) with contributions from the National Technical University of Athens (NKUA), Greece, and the Max Planck Institute for Plasma Physics (IPP), Germany [6-7]. In support to the development of the CW prototype, a short-pulse pre-prototype gyrotron was developed at KIT. The electron optics and RF design is identical in the two gyrotrons, allowing for experimental validation of the design in ms pulses before the final construction of the CW prototype. This validation was indeed achieved by the first experimental campaign with the short-pulse pre-prototype, which took place at KIT in August-September 2020 and produced excellent results [8]. Stable operation in the design cavity mode $TE_{28,10}$ was demonstrated in 0.5-1 ms pulses, while the output power reached 1.6 MW with 30% efficiency in non-depressed collector operation. In depressed collector operation an efficiency of 44% was achieved at the nominal power of 1.5 MW and an efficiency above 46% was possible at 1.1 MW.

In the present paper, the experimental behavior of the 1.5 MW 140 GHz short-pulse pre-prototype at a multitude of operation points is analyzed by detailed multifaceted simulations. The simulations address the applied magnetic field, the electron beam formation and properties, the beam-wave interaction, the Ohmic losses, the function of the quasi-optical output coupler of the gyrotron, and the properties of the gyrotron window. For the simulation-experiment comparison the experimental uncertainties are also discussed. Moreover, in contrast to the usual practice, the possibility of parasitic after-cavity interaction in the gyrotron launcher as well as the possibility of parasitic mode excitation in the cavity at a

Manuscript submitted March 12, 2021. This work has been carried out within the framework of the EUROfusion Consortium and has received funding from the Euratom research and training programme 2014–2018 and 2019–2020 under grant agreement No. 633053. The views and opinions expressed herein do not necessarily reflect those of the European Commission.

K. A. Avramidis, Z. C. Ioannidis, S. Illy, J. Jin, T. Ruess, M. Thumm, and J. Jelonnek are with Karlsruhe Institute of Technology, Institute for Pulsed Power and Microwave Technology, Karlsruhe, 76131 Germany. (e-mail: konstantinos.avramidis@ kit.edu).

G. Aiello is with Karlsruhe Institute of Technology, Institute of Applied Materials, Karlsruhe, 76131 Germany.

frequency band extending down to 120 GHz are investigated.

The motivation for this work is twofold: first, it is well known that the development of high-power gyrotrons is heavily relying on accurate simulations, as far as the design of components, the identification of appropriate operating regimes, and the interpretation of experimental results are concerned. The comparison between simulation and experiment is therefore indispensable for the validation of the simulation procedures and tools. Second, an agreement between simulation and experiment, suggesting that the gyrotron behaves as expected, provides also a powerful validation of the gyrotron design and fabrication. In this sense, the present paper is complementing the experimental findings and design validation given in [8].

The paper is organized as follows: the multifaceted simulation procedure and tools are described and discussed in section II. Then, the simulation-experiment comparison is detailed in section III. Section IV recapitulates the conclusions of this work.

II. Multifaceted Simulation Procedure and Tools

Three different groups of experimentally achieved 0.5 ms pulses with the 1.5 MW 140 GHz $TE_{28,10}$ short-pulse gyrotron were considered for simulation. The operation was without collector depression and the three groups of pulses correspond to three different magnetic field profile cases. The field profile of the super-conducting Oxford Instruments magnet used in the experiments is controlled by the values of two coil currents, applied to the main coil and the gun coil, respectively. The coil currents for the three cases are given in Table I.

TABLE I
EXPERIMENTAL CASES CONSIDERED (MAGNETIC FIELD PROFILES)

Case	Coil currents		Calculated quantities at the cavity		
	Main (A)	Gun (A)	Magnetic field (T)	*e*-beam radius (mm)	Guiding-center spread (mm)
1	48.786	8.667	5.54	10.32	0.35
2	48.436	8.542	5.50	10.30	0.35
3	48.975	8.329	5.56	10.19	0.35

A. Magnetic field profile and electron beam properties

From the coil geometry of the super-conducting magnet (as provided in the construction file [9]) and from the coil currents, the magnetic field profile along the gyrotron was calculated using the in-house electron beam optics code ESRAY [10]. In addition to the magnetic field value at the gyrotron cavity, ESRAY also provides the corresponding electron beam radius and the uniform guiding-center spread (Table I). For each of the three cases and for several experimentally measured values of the applied accelerating voltage and of the beam current, ESRAY calculated also the values (at the cavity) of the beam kinetic energy and of the electron velocity ratio α, together with the corresponding rms spreads. As an example, the results for case 1 are shown in Fig. 1. It should be noted that the calculation assumes no neutralization of the electron beam space charge during the pulse length of 0.5 ms. This is supported by the fact that, for the pulses considered in this paper, there was no experimental indication of neutralization onset. The absence of neutralization explains the ~7-8 keV lower electron kinetic energy with respect to the accelerating voltage, associated with the space-charge depression.

B. Beam-wave interaction

The interaction of the electron beam with the resonant TE modes in the gyrotron cavity has been simulated by the time-dependent, multi-mode, in-house code EURIDICE [11]. A slow-variables self-consistent model, similar to that of [12], is implemented. Also, the Vlasov approximation is adopted, i.e. the weak mode conversion due to the mild axial inhomogeneity, introduced by the changing cavity radius, is neglected [13]. Nonetheless, EURIDICE incorporates some advanced features, like the improvements with respect to the reference frequencies described in [14], the consideration of the influence of the axial variation of the magnetostatic field on the beam radius and axial electron momentum, and finally the consideration of the change of the electron energy and axial momentum due to the change of the space-charge depression along the beam path. (This change is introduced by the varying distance between the beam and the cavity wall along the beam path.)

The selection of the cavity TE modes, which are considered in the multi-mode interaction simulation, is based on criteria related to the electron cyclotron frequency and the beam-wave coupling coefficient. In particular, as a usual practice, the selected modes have resonant frequencies in the range of ±5% of the electron cyclotron frequency values (to take account of the cyclotron resonance band), and coupling coefficient greater than 50% of that of the operating $TE_{28,10}$ mode. (According to our experience with multi-mode simulations, the inclusion of modes with even weaker coupling does not alter the result because they are suppressed by the modes with stronger coupling.) The above criteria resulted in a large number of competing modes in the 133-161 GHz frequency range.

Two domains, as shown in Fig. 2, have been considered for the beam-wave interaction simulations. The first is the cavity and non-linear uptaper region, which is the usual simulation domain. The second is the complete region of the cavity, non-linear uptaper, and launcher. EURIDICE calculates the RF power radiated out of the simulation domain, taking as input the

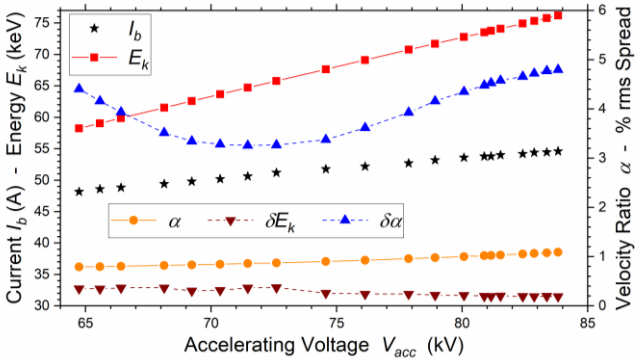

Fig. 1. Calculated electron beam properties in the gyrotron cavity for several experimentally measured values of the applied accelerating voltage V_{acc} (abscissa) and of the beam current I_b (stars), for the magnetic field profile of case 1: electron kinetic energy E_k, electron velocity ratio α, % rms energy spread δE_k, and % rms velocity ratio spread $\delta\alpha$.

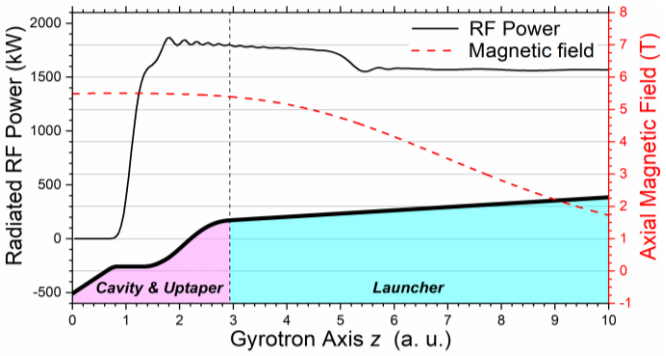

Fig. 2. Radius contour of the cavity, non-linear uptaper, and launcher (thick black line). Calculation of radiated RF power along the gyrotron axis for case 2 of Table I with V_{acc} = 81.3 kV and I_b = 64 A, where a 13% power drop due to after-cavity interaction in the launcher (at z ~ 5-6) is evident.

calculated magnetic field profile and electron beam properties from ESRAY (including spreads in energy, velocity, and guiding-center) as well as the list of competing TE modes.

The reason for simulating the beam-wave interaction also in the launcher is to take into account the possibility of static after-cavity interaction (ACI) that degrades the gyrotron efficiency [15-16]. An example is shown in Fig. 2: the simulation by EURIDICE predicts a 13% drop in radiated power due to ACI in the launcher. In section III, EURIDICE results for both simulation domains are compared with the experiment and the importance of after-cavity interaction is further discussed.

It should be noted that in the launcher region the Vlasov approximation is, in principle, not valid because the wall has mode-converting perturbations for the transformation of the operating $TE_{28,10}$ mode to a linearly polarized, fundamental Gaussian beam. However, in EURIDICE (as well as in [15-16]) this approximation is still kept and the launcher is modelled as an azimuthally symmetric smooth tapered section. This is in line with the studies in [17-18], where it was shown that the difference in the results if the mode conversion in the launcher is indeed taken into account is small. This is because the coupling of the RF field to the electron beam at the position of the after-cavity interaction is similar for both cases, i.e. the case where mode conversion is considered in the transverse RF field pattern, and the case where the transverse RF field pattern is approximated by that of the operating TE mode only.

C. Calculation of losses

For comparing simulation and experiment, a careful calculation of the various losses in the gyrotron is necessary. We can distinguish three types of losses, namely Ohmic losses, diffraction losses, and losses at the output window.

The Ohmic losses in the cavity and non-linear uptaper are calculated by EURIDICE, using the well-known formula for the surface density ρ of Ohmic losses [19]:

$$\rho = \frac{1}{2\sigma\delta}\left|\mathbf{H}_t\right|^2 \tag{1}$$

Here, $\mathbf{H}_t$ is the component of the high-frequency (RF) magnetic field that is tangential to the metallic wall, σ is the electrical conductivity of the wall, and $\delta = [2/(\mu\sigma\omega)]^{1/2}$ is the skin depth. For the calculation, the electrical conductivity σ =5.8×10^7 S/m of copper at room temperature is used because, at the experimental pulse length of 0.5 ms, the rise of the wall temperature and the cavity thermal expansion can be neglected [20]. Also, a correction factor for the losses, due to a typical 0.1 μm rms surface roughness, is taken into account by the Hammerstad/Bekkadal formula [21] and is inserted in (1) as a multiplication factor. The Ohmic losses in the quasi-optical system (i.e. launcher and three mirrors) are calculated using the same principle by the in-house code TWLDO for quasi-optical system design.

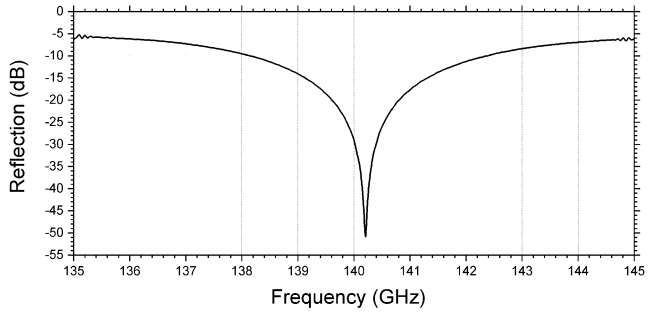

Fig. 3. Reflection of the gyrotron output window versus frequency, as measured at the KIT test-bench before installing the window in the gyrotron.

The diffraction losses in the quasi-optical system (stray radiation in the mirror box) are calculated by the commercial code SURF3D. Additional (small) diffraction losses originate from the mild mode conversion of the cavity TE mode at the cavity down-taper (i.e. before the cylindrical part) and at the non-linear uptaper. Such mode conversion losses are calculated by the in-house scattering matrix code MCONV [22].

The window losses comprise the dielectric losses and the losses due to reflection. The window disk of the short-pulse gyrotron is made of Infrasil 302. The dielectric constant of this material is ε_r = 3.81 and its loss tangent was measured at KIT as tanδ ~ 4×10^{-4}. The ratio of the dielectric losses P_{abs} to the incident power P_{in} at the window are calculated using the formula (4.1) in [23]:

$$\frac{P_{abs}}{P_{in}} = \frac{d}{\lambda}\pi\left(1+\varepsilon_r\right)\tan\delta \tag{2}$$

where d is the window thickness and λ is the free-space wavelength.

The reflection curve of the window disk was measured at KIT prior to its installation in the tube. The set-up [24] uses a network analyser PNA5222B and WR5 extension modules. The RF beam is radiated by a corrugated horn antenna and is focussed on the center of the window using two mirrors. A semi-transparent Mylar foil is used to separate the transmitting and receiving path. The receiving antenna is again a corrugated horn antenna. The result is shown in Fig. 3 and allows to determine the reflection losses that correspond to the measured frequency of the RF beam generated by the gyrotron.

The calculated losses between the gyrotron cavity and window are summarized in Table II for the operating $TE_{28,10}$ mode as well as for the competing $TE_{29,10}$ mode, which has also

TABLE II
GYROTRON LOSSES BETWEEN NON-LINEAR UPTAPER AND WINDOW

Losses type	Losses percentage (%)	
	$TE_{28,10}$ (140.25 GHz)	$TE_{29,10}$ (142.91 GHz)
Ohmic losses at launcher	1.32	1.28
Ohmic losses at three mirrors	0.35	0.34
Stray radiation in mirror box	1.65	2.30
Mode conversion losses at cavity and non-linear uptaper	0.24	0.24
Window absorption	1.86	1.90
Window reflection	0.007	13.9
Total losses	*5.43*	*19.96*

been excited in the experiment. The frequencies used for determining the losses were those measured experimentally during the operation of the gyrotron. To compare the simulation results with the experimental measurements, the radiated power calculated by EURIDICE is reduced by the percentage of total losses given in the last line of Table II.

III. COMPARISON BETWEEN SIMULATION AND EXPERIMENT

Following the multifaceted simulation procedure detailed in Section II, the simulation results on the expected RF power at the gyrotron window were compared with the RF power measured at the short-pulse load adjacent to the window. The comparison was made for all three magnetic field profile cases of Table 1, considering a multitude of values of accelerating voltage and beam current. It should be noted that in cases 1 and 2 no parasitic oscillations were observed experimentally. In case 3, however, parasitic oscillations in the frequency range 130-134 GHz appeared at high values of the acceleration voltage (i.e. above 83 kV).

A. Cases without parasitic oscillations

The comparison between simulation and experiment for the cases 1 and 2 of Table 1, where no parasitic oscillations were experimentally observed, is shown in Fig. 4. The error bars at the experimental points for the power represent a ±5% and ±1% uncertainty in the measurement of the power and voltage, respectively. This and the following figures focus on the voltage values for which we have experimental measurements. The simulation results are shown both for the case where the beam-wave interaction domain is only the cavity and non-linear uptaper (thus excluding after-cavity interaction in the launcher) and for the case where the interaction domain incorporates also the launcher and therefore the possibility of ACI there.

The last experimental points at high voltage correspond to the limit after which the operating $TE_{28,10}$ mode is lost. A first observation in Fig. 4 is that the simulated loss of the operating mode occurs at 1-2 kV higher voltage compared to the voltage of the experimental mode loss. This can be attributed to the possibility that, during the experiment, the magnetic field values were slightly lower than those calculated in Table 1, given that the measurement uncertainty in the currents of the magnet coils is ±0.1%. This motivated the repetition of the simulations of Fig. 4, assuming magnetic field values in the cavity that are 0.1 % lower than the values of Table 1. The

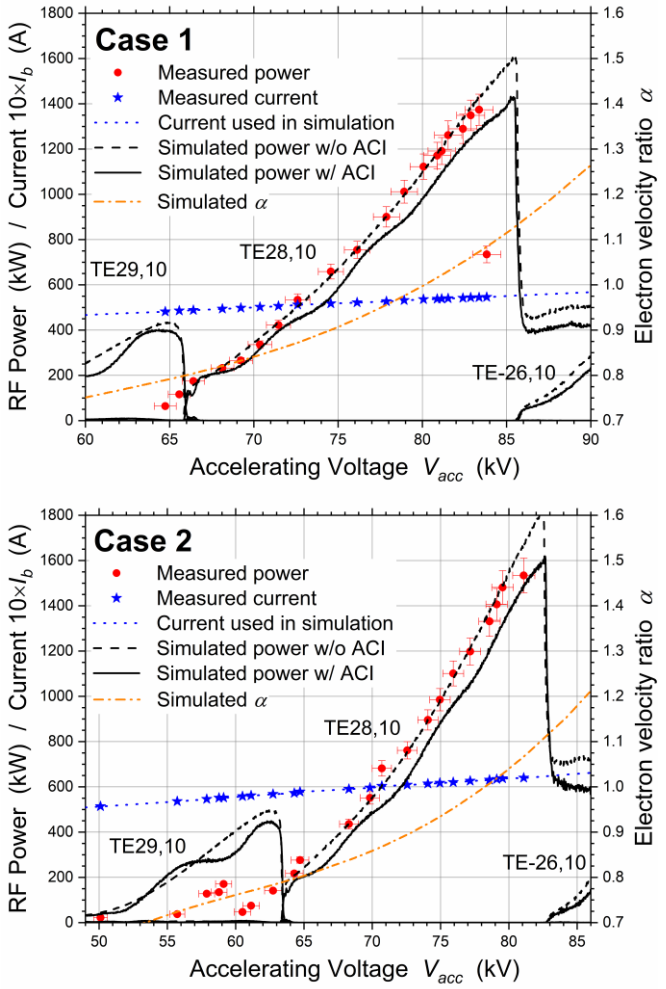

Fig. 4. Comparison of experimental and simulation results on the RF power at the gyrotron window for case 1 (top) and case 2 (bottom) of the magnetic field profile, as defined in Table 1. Simulation results with and without consideration of the after-cavity interaction (ACI) in the launcher are shown. The measured current and the current values used in the simulations are also shown, together with the calculated electron velocity ratio α. The interaction simulations considered 83 competing TE modes in the frequency range 133.5-154.3 GHz. (A negative azimuthal index denotes a counter-rotating mode.)

results are shown in Fig. 5, where an excellent agreement between experiment and simulation is demonstrated with respect to the operating $TE_{28,10}$ mode.

A discrepancy still remains in case 2, where the competing $TE_{29,10}$ mode was also excited experimentally: the simulated mode loss for $TE_{29,10}$ occurs at 3 kV higher voltage compared to the experiment and the simulated power is higher than the measured one. Both of these effects can be attributed to a reduced quality of the electron beam when $TE_{29,10}$ is excited. An explanation could be the high stray RF power associated with the competing $TE_{29,10}$ mode. According to Table II, the stray RF power in the gyrotron is the sum of stray radiation in the mirror box, mode conversion, and window reflection (lines 3, 4, and 6, respectively). This power is calculated to be ~32 kW at 1.6 MW window power for the operating $TE_{28,10}$ mode, and ~62 kW at 300 kW window power for the $TE_{29,10}$ mode. The significantly higher stray RF power associated with the observed excitation of the $TE_{29,10}$ mode could lead to deteriorating vacuum conditions in the vicinity of the electron

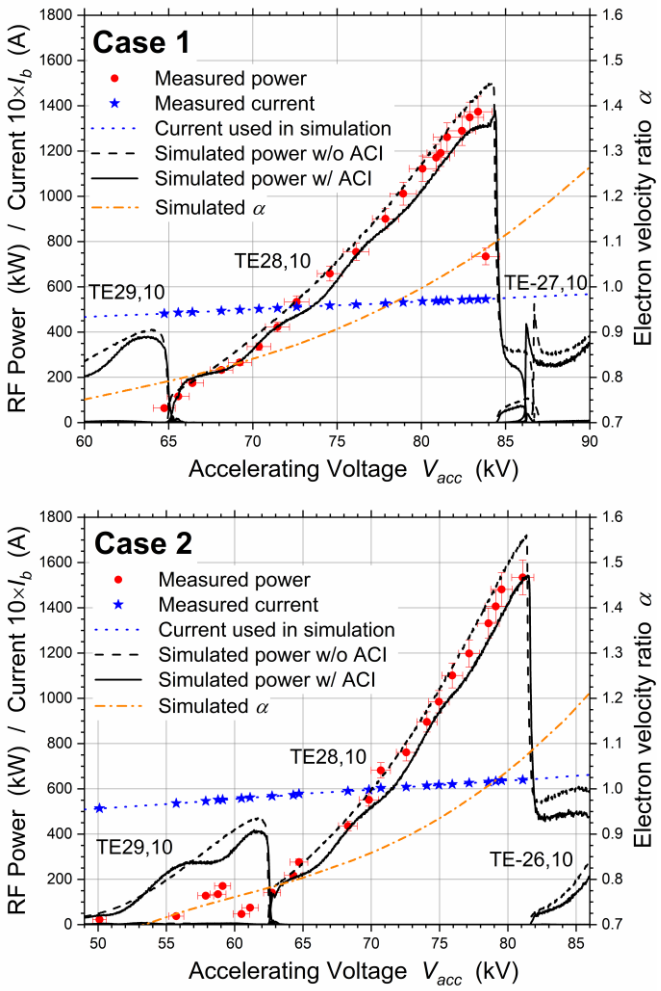

Fig. 5. Repetition of the simulations of Fig. 4, assuming 0.1% lower values for the magnetic field in the cavity, in line with the measurement uncertainty of the magnet coil currents. An excellent agreement between experiment and simulation has been achieved with respect to the operating $TE_{28,10}$ mode.

beam (in the cavity and before) that reduce the beam quality.

Coming to the possibility of after-cavity interaction, the simulation result when ACI is considered is visibly different from the result when it is ignored. However, as it is apparent from Fig. 5, both results lay more or less within the experimental error bar. Nonetheless, a closer inspection of the simulation curves favors the modelling with ACI inclusion, because, in this case, the simulation curve exhibits undulations, which are also present in the experimental results. These undulations reflect the different intensity of ACI at different voltage values.

For the case 2 of the magnetic field profile, the frequency of the operating $TE_{28,10}$ mode as well as that of the competing $TE_{29,10}$ mode were measured. The measurements are shown in Fig. 6, including an error bar of ±10 MHz, and are compared to the simulation result, which corresponds to the simulation of Fig. 5(bottom). An offset of ~110 MHz between simulation and experiment is apparent. This can be easily explained if it is assumed that the cavity radius at the midsection is 19 μm larger that the design value. The simulated frequency under this assumption is also shown in Fig. 6 and an excellent agreement with the experiment is achieved (save for the voltage value

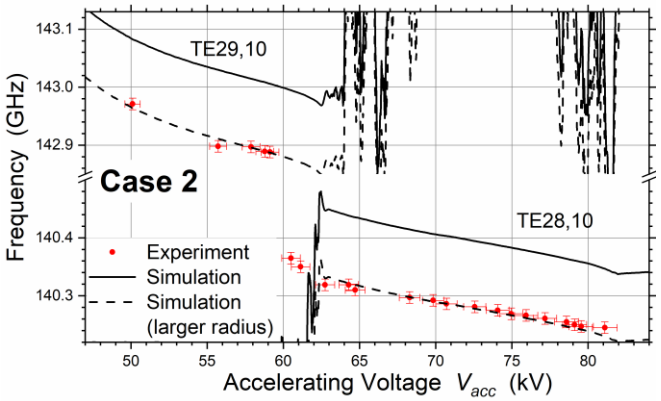

Fig. 6. Measured and simulated frequency for case 2 of the magnetic field profile. The simulation result (solid curve) corresponds to that of Fig. 5(bottom). The ~110 MHz offset between simulation and experiment can be eliminated if a 19 μm larger cavity radius is assumed (dashed curve).

where $TE_{29,10}$ is lost, as discussed earlier). The assumption of 19 μm larger cavity radius is in line with the known ±20 μm manufacturing accuracy of the cavity radius. In addition, some minor thermal expansion of the uncooled cavity during the 0.5 ms pulses, of the order of a few μm, cannot be excluded.

In conclusion, for the two magnetic field profile cases where no parasitic oscillations are detected, careful multifaceted modeling and observation of the measurement and manufacturing uncertainties can achieve a very good agreement between simulation and experiment, over a wide range of parameters.

B. Case with parasitic oscillations

For the case 3 of the magnetic field profile in Table 1, parasitic oscillations in the frequency range 130-134 GHz were experimentally observed when the acceleration voltage V_{acc} exceeded 83 kV. The onset of parasitic oscillations was accompanied by a saturation in output power, as shown in Fig. 7. In gyrotrons, the RF parasitic oscillations that limit the power and appear at frequencies 5-15% lower than the operating frequency are attributed, as a rule, to parasitic beam-wave interaction in the beam tunnel before the cavity (e.g. [25-29]). It can be argued that the onset of parasitic excitation in case 3 is related to the higher values of the electron velocity ratio ($\alpha > 1.25$), as compared to cases 1 and 2.

Since the multifaceted modeling described in this work does not take into account the possibility of parasitic mode excitation in the beam tunnel, a discrepancy between simulation and experiment is expected when such excitation occurs. This is apparent in Fig. 7, where the simulation predicts higher power than experimentally measured for $V_{acc} > 83$ kV. On the other hand, in the absence of parasitic oscillations ($V_{acc} < 83$ kV), a very good agreement between simulation and experiment is again demonstrated. In line with the discussion in section IIIA, the magnetic field assumed in the simulation is 0.1% lower than that of Table 1. Also, the simulation curve that considers after-cavity interaction in the launcher resembles better the undulations in the measured power. These observations in the absence of parasitic oscillations consolidate further the conclusion of section IIIA.

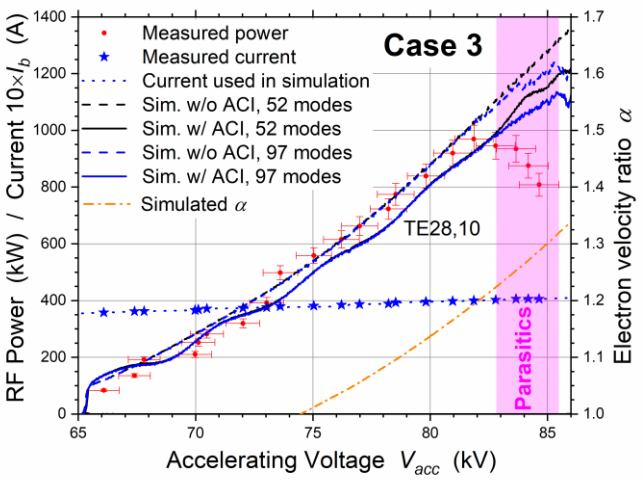

Fig. 7. Comparison of experimental and simulation results on the RF power at the gyrotron window for case 3 of Table 1, assuming 0.1% lower cavity magnetic field. The voltage region of experimentally observed parasitic oscillations is shadowed. Simulation results with and without consideration of the after-cavity interaction (ACI) in the launcher are shown. The calculated electron velocity ratio α is also shown. The interaction simulations consider either 52 competing TE modes in the "standard" 133.6-160.7 GHz frequency range (black curves), or 97 modes in the extended 120.0-160.7 GHz frequency range (blue curves). In the latter case, a power reduction above 83 kV is visible in the simulation curves.

Although the primary explanation with respect to the origin of parasitic oscillations is the beam tunnel, the possibility that their origin is a backward wave excitation in the cavity or beyond was also examined. To do this, the simulations were repeated with an increased number of 97 competing modes, covering the extended frequency range of 120.0-160.7 GHz. The new results are also shown in Fig. 7, in direct comparison to the initial results with 52 modes. The simulations are identical up to V_{acc} ~ 83 kV but, at higher voltage, the power in the simulations with 97 modes is reduced compared to that of the simulations with 52 modes.

The power reduction comes from the excitation of parasitic modes. This is clearly visible in Fig. 8(top) where the simulated power with 97 modes is shown in logarithmic scale. Above 83 kV there is excitation, at a power level of ~3 kW, of the $TE_{24,9}$ mode at 127.9 GHz and of the$TE_{26,9}$ mode at 130.9 GHz. Notably, the voltage range of the parasitic mode excitation coincides with that in the experiment. Moreover, the parasitic frequencies in the simulation are very close to the frequency range of the experimentally observed parasitic oscillations. It should be noted here that the experimental diagnostic was a filter bank and the parasitic signals appeared in the channel corresponding to the 130-134 GHz frequency range. Hence, no exact measurement of the parasitic frequency was available.

Despite the simulated parasitic mode excitation above 83 kV, however, the simulated power still remains significantly higher than the measured power. This may be explained by the argument that generation of backward waves in the 3 kW level in the cavity could increase the stray RF power in the tube (by a possible coupling with beam-tunnel modes), thus disrupting the good vacuum conditions and resulting in a decline in electron beam quality and interaction efficiency. This effect is not considered in the simulation, of course.

The simulation result with extended mode list, suggesting parasitic mode excitation in the cavity (or after) at a voltage range and at frequencies close to what was experimentally observed, is very interesting and broadens the possibilities with respect to the origin of parasitic oscillations in gyrotrons. To consolidate this argument, however, it has to be verified that the simulations with extended mode list do not predict parasitic mode excitation also for the cases where no parasitics were experimentally observed. Therefore, the simulations for cases 1 and 2 were repeated with a larger number of competing modes,

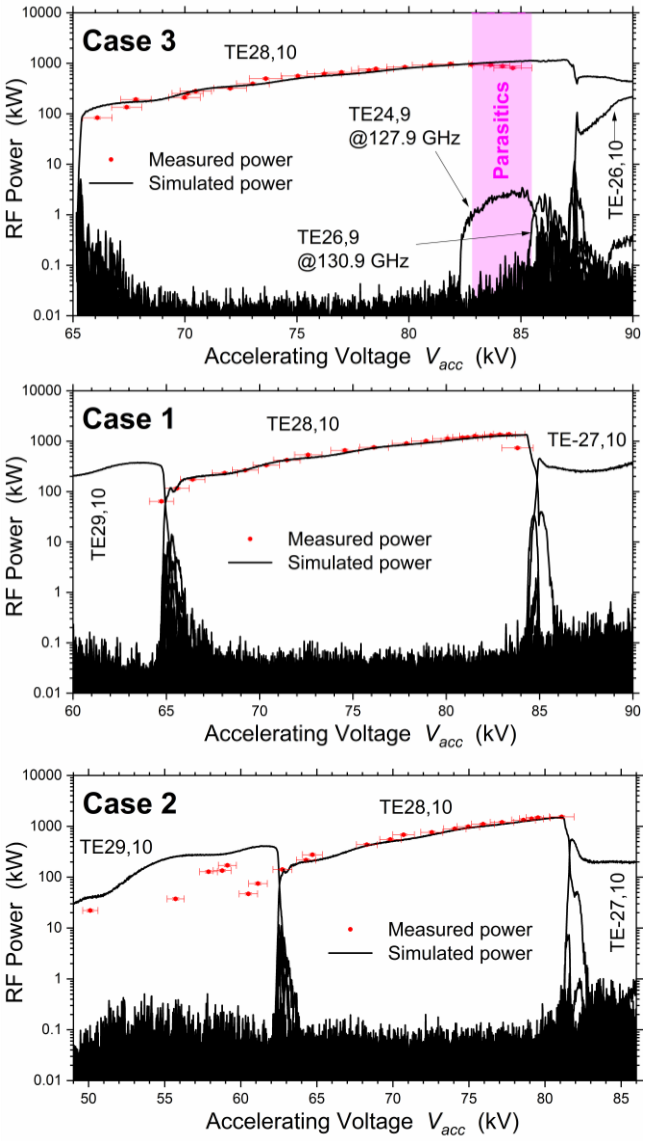

Fig. 8. Comparison of experimental and simulation results on the RF power at the gyrotron window for cases 1-3 of Table 1, assuming 0.1% lower cavity magnetic field and considering an extended list of competing modes. Top: case 3 with 97 competing modes in the 120.0-160.7 GHz range. The voltage region of experimentally observed parasitic oscillations is shadowed and coincides with the region of parasitic excitation predicted by the simulations. Middle and bottom: case 1 and case 2, respectively, with 99 competing modes in the 120.0-160.7 GHz range. In these two cases, the simulations do not predict parasitic mode excitation, as the power level of the competing modes remains at a ~0.1 kW noise level. This is again in agreement with the experimental findings. For clarity, in all three cases only the simulations with consideration of the after-cavity interaction (ACI) in the launcher are shown. The simulations without consideration of launcher interaction are similar with respect to the excitation of parasitic modes.

covering the 120.0-160.7 GHz frequency range. The results are also shown in Fig. 8. Indeed, despite the increased number of modes and frequency range, no parasitic excitation takes place and the results remain practically identical to those of Fig. 5.

IV. Summary and Conclusions

A multifaceted simulation procedure, based primarily on in-house codes, has been used for the simulation of the experimental operation of the 1.5 MW 140 GHz short-pulse pre-prototype gyrotron for W7-X. An excellent reproduction of experimental results, with respect to the excitation and power levels of the operating $TE_{28,10}$ mode, has been demonstrated by simulation for a large number of operating points at different magnetic field profiles and electron beam parameters. This simulation-experiment agreement has been achieved solely by the numerical modeling and the consideration of the experimental uncertainties, without resorting to any arbitrary speculations, e.g. about the electron beam properties or the internal losses. In addition, any discrepancies observed between simulation and experiment are exclusively associated with the excitation of parasitic modes or competing modes and can be expected because they are caused by phenomena not addressed by the employed simulation tools. Such phenomena are the excitation of parasitic modes in the beam tunnel or the increased stray RF power levels and vacuum deterioration in the tube. The above findings validate the multifaceted simulation procedure as a powerful means for gyrotron design and interpretation of experimental results.

Additional findings of this study have been the following: (i) The 1.5 MW 140 GHz pre-prototype gyrotron for W7-X behaves as simulated. This, combined with the fact that the gyrotron achieved the targeted performance of efficient 1.5 MW operation [8], verifies the beam optics and RF design as well as the correct fabrication and alignment of the tube components. (ii) Although the simulation results with and without consideration of possible after-cavity interaction (ACI) in the gyrotron launcher are within the error bar of the experimental results, the shape of the experimental power curves resembles better that of the simulation curves when ACI is considered. This is an indirect indication of ACI occurrence in reality. (iii) Excitation of parasitic backward waves in the cavity and non-linear uptaper, at frequencies and voltage values compatible with the experimental observations, has been demonstrated in simulation and is triggered by higher values of the electron velocity ratio. This adds an additional possibility, besides the beam tunnel, regarding the origin/support of deleterious parasitic oscillations in high power gyrotrons at frequencies 5-15% lower than nominal.

Acknowledgment

The authors would like to thank Andreas Meier (KIT, Institute of Applied Materials) for providing the Infrasil 302 loss tangent data as well as Dr. Andreas Dinklage (IPP) for fruitful discussions. Part of the simulations was performed on the EUROfusion High Performance Computer (Marconi-Fusion).

References

[1] T. Klinger *et al*., "Overview of first Wendelstein 7-X high-performance operation," *Nuclear Fusion*, vol. 59 pp. 112004, Jun. 2019. https://doi.org/10.1088/1741-4326/ab03a7

[2] R. C. Wolf *et al*., "Performance of Wendelstein 7-X stellarator plasmas during the first divertor operation phase," *Phys. Plasmas*, vol. 26, pp. 082504, Aug. 2019. https://doi.org/10.1063/1.5098761

[3] A. Dinklage *et al*., "Magnetic configuration effects on the Wendelstein 7-X stellarator," *Nature Physics*, vol. 14, pp. 855-860, Aug. 2018. https://doi.org/10.1038/s41567-018-0141-9

[4] Yu. Turkin *et al*., *in preparation*.

[5] R. C. Wolf *et al*., "Electron-cyclotron-resonance heating in Wendelstein 7-X: A versatile heating and current-drive method and a tool for in-depth physics studies," *Plasma Phys. Controlled Fusion*, vol. 61, pp. 014037, Nov. 2018. https://doi.org/10.1088/1361-6587/aaeab2

[6] K. A. Avramidis *et al*., "Towards a 1.5 MW, 140 GHz gyrotron for the upgraded ECRH system at W7-X," *Fus. Eng. Des.*, vol. 163, pp. 112173, Mar. 2021. https://doi.org/10.1016/j.fusengdes.2020.112173

[7] K. A. Avramidis *et al*., "Studies towards an upgraded 1.5 MW gyrotron for W7-X," *EPJ Web Conf*., vol. 203, pp. 04003, Mar. 2019. https://doi.org/10.1051/epjconf/201920304003

[8] Z. C. Ioannidis, K. A. Avramidis, T. Rzesnicki, I. Chelis, G. Gantenbein, S. Illy, J. Jin, I. Gr. Pagonakis, M. Thumm, J. Jelonnek, "Generation of 1.5MW-140GHz ms pulses with the modular pre-prototype gyrotron for W7-X", *IEEE Electron Device Lett.*, Apr. 2021, https://doi.org/10.1109/LED.2021.3073221, [Online].

[9] Superconducting Magnet System Operator's Manual, Project No. 44305, Oxford Instruments Superconductivity, Abingdon., Oxon, United Kingdom, 2000.

[10] S. Illy, J. Zhang, and J. Jelonnek., "Gyrotron electron gun and collector simulation with the ESRAY beam optics code," *IVEC 2015*, Beijing, China, 2015. http://doi.org/10.1109/IVEC.2015.7223779

[11] K. A. Avramides, I. G. Pagonakis, C. T. Iatrou, and J. L. Vomvoridis, "EURIDICE: A code-package for gyrotron interaction simulations and cavity design," in *Proc. EPJ Web Conf*., vol. 32. Sep. 2012, p. 04016. http://dx.doi.org/10.1051/epjconf/20123204016

[12] N. S. Ginzburg, G. S. Nusinovich, and N. A. Zavolsky, "Theory of non-stationary processes in gyrotrons with low Q resonators," *Int. J. Electronics*, vol. 61, no. 6, pp. 881-894, Jun. 1986. https://doi.org/10.1080/00207218608920927

[13] E. Borie and O. Dumbrajs, "Calculation of eigenmodes of tapered gyrotron resonators," *Int. J. Electronics*, vol. 60, no. 2, pp. 143-154, 1986. https://doi.org/10.1080/00207218608920768

[14] K. A. Avramidis, "Investigations and advanced concepts on gyrotron interaction modeling and simulations," *Phys. Plasmas*, vol. 22, 123114, Dec. 2015. https://doi.org/10.1063/1.4938043

[15] V. E. Zapevalov and M. A .Moiseev, "Influence of aftercavity interaction on gyrotron efficiency," *Radiophys. Quantum Electronics*, vol. 47, pp. 520-527, Jul. 2004. https://doi.org/10.1023/B:RAQE.0000047243.18212.1d

[16] E. M. Choi, M. A. Shapiro, J. R. Sirigiri, and R. J. Temkin, "Experimental observation of the effect of aftercavity interaction in a depressed collector gyrotron oscillator," *Phys Plasmas*, vol. 14, 093302, Sep. 2007. https://doi.org/10.1063/1.2776911

[17] M. Obermaier, "Theoretical investigation on the possibility of parasitic particle-wave interaction in the gyrotron launcher," M.S. thesis, IHM, KIT, Kalrsruhe, Germany, Nov. 2018.

[18] K. A. Avramidis, M. Obermaier, J. Jin, A. Marek, I. Gr. Pagonakis, M. Thumm, S. Illy, and J. Jelonnek, "Beam-wave interaction modelling in the gyrotron launcher," presented at the *31st Joint Russian-German Workshop on ECRH and Gyrotrons*, Lenggries, Germany, June 3–8, 2019.

[19] J. D. Jackson, "Wave guides and resonant cavities," in *Classical Electrodynamics*, 2nd ed., Wiley, 1975, ch. 8, sec. 8.1, p. 339.

[20] K. A. Avramidis, A. Bertinetti *et al*., "Numerical studies on the influence of cavity thermal expansion on the performance of a high-power gyrotron," *IEEE Trans. Electron Devices*, vol. 65, no. 6, pp. 2308 - 2315, Jun. 2018. https://doi.org/10.1109/TED.2017.2782365

[21] L. Tsang, H. Braunisch, R. Ding, and X. Gu, "Random rough surface effects on wave propagation in interconnects," *IEEE Trans. Adv. Packag*. vol. 33, no. 4, pp. 839 - 856, Dec. 2010. https://doi.org/10.1109/TADVP.2010.2089789

[22] O. Hoechtl, "Numerische Analyse der Modekonversion in Koaxialen Wellenleiter-komponeneten," Diploma Thesis, KfK5298, Kalrsruhe University, Germany, Feb. 1994.

[23] H.-U. Nickel and M. Thumm, "Plane transverse waveguide windows – Survey of formulas for reflection, transmission, and absorption," *16th Int. Conf. Infr. Mill. Waves*, Lausanne, Switzerland, 1991, pp. 444–445. https://doi.org/10.1117/12.2297936

[24] T. Ruess, G. Gantenbein , Z. Ioannidis, T. Rzesnicki, D. Wagner, M. Thumm, J. Jelonnek, "Frequency measurement techniques for megawatt-class gyrotrons," *tm-Technisches Messen*, 2021, *under review*

[25] I. I. Antakov, I. G. Gachev, and E. V. Zasypkin, "Self-excitation of spurious oscillations in the drift region of gyrotrons and their influence on gyrotron operation," *IEEE Trans. Plasma Sci*., vol. 22, no. 5, pp. 878–882, Oct. 1994. https://doi.org/10.1109/27.338303

[26] M. Pedrozzi, S. Alberti, J. P. Hogge, M. Q. Tran, and T. M. Tran, "Electron beam instabilities in gyrotron beam tunnels," *Phys. Plasmas*, vol. 5, no. 6, pp. 2421–2430, Jun. 1998. https://doi.org/10.1063/1.872918

[27] K. Sakamoto *et al*., "Development of 170 and 110 GHz gyrotrons for fusion devices," *Nucl. Fusion*, vol. 43, no. 8, pp. 729–737, Aug. 2003. https://doi.org/10.1088/0029-5515/43/8/314

[28] G. Gantenbein *et al*., "Experimental investigations and analysis of parasitic RF oscillations in high-power gyrotrons," *IEEE Trans. Plasma Sci*., vol. 38, no. 6, pp. 1168–1177, Jun. 2010. https://doi.org/10.1109/TPS.2010.2041366

[29] Z. C. Ioannidis, I. Chelis, G. Gantenbein, T. Rzesnicki, and J. Jelonnek, "Experimental classification and enhanced suppression of parasitic oscillations in gyrotron beam tunnels," *IEEE Trans. Electron Devices*, vol. 67, no. 12, pp. 5783-5789, Dec. 2020. https://doi.org/10.1109/TED.2020.3025751